7

Uncertainties in Estimating Magma Source Parameters from InSAR Observation

Wenyu Gong,[1] Zhong Lu,[2] and Franz Meyer[1]

ABSTRACT

Satellite radar interferometry (InSAR) has been proven to be an essential technique for measuring volcano-wide surface deformations at a spatial resolution of tens of meters and centimeter-level accuracy. For many volcanic systems, InSAR observations have been the main data source for studying geophysical processes at active volcanoes and are used frequently to estimate volcano source parameters using inverse modeling techniques. This chapter evaluates how the accuracy of estimated source model parameters is affected by typical errors in radar phase measurement such as baseline-induced phase signals, atmospheric distortions, and decorrelations noise. To mathematically study the influence of these errors, we use the Mogi source model as example and discuss how the different error components in InSAR deformation measurement affect the uncertainties of estimated source model parameters. To understand this inherent processes, nonlinear least squares and Monte Carlo simulations are used to generate the posterior probability distribution of source parameters. In addition, the impact of approximations in the Mogi source model are also discussed in this paper, including the flat-surface assumption, the disregard of magma compressibility, and the Poisson's ratio.

7.1. INTRODUCTION

There are approximately 1500 volcanoes on Earth that have erupted in the past 10,000 years. Today volcanic activity affects the lives and livelihoods of a rapidly growing number of people around the globe. About 20 volcanoes are erupting on Earth at any given time; 50–70 erupt each year, and about 160 erupt each decade [*GVP*, 2015]. Volcano monitoring is key to mitigating the adverse impacts of volcanic activity [*VHP*, 2015]. In general, the "eruption cycle" of a volcano can be conceptualized as a series of events from deep magma generation to surface eruption, including such stages as partial melting, initial ascent through the upper mantle and lower crust, crustal assimilation, magma mixing, degassing, shallow storage, and finally ascent to the surface [*Dzurisin*, 2003; 2007]. This process is complex, varying from one eruption to the next and from volcano to volcano. In many cases, volcanic eruptions are preceded by pronounced ground deformation in response to increasing pressure from magma chambers or due to the upward intrusion of magma. Therefore, monitoring and modeling volcanic deformation constitutes a critical element in providing warning of impending eruptions, reducing loss of life, and mitigating impact on property [*Dzurisin*, 2007].Together with seismology, continuous ground deformation measurements (like GPS), geology/petrology, and gas geochemistry observations, the spatially dense deformation field derived satellite interferometric synthetic aperture radar (InSAR) can play a pivotal role in constraining the most important parameters needed to assess short-term volcanic hazards and better understand volcanic processes.

InSAR imaging of ground surface deformation is contaminated by multiple error sources, (e.g., atmospheric artifacts), contributions from inaccurate satellite orbit and auxiliary topography model, reducing the sensitivity

[1]*Geophysical Institute, University of Alaska Fairbanks, Fairbanks, Alaska, USA*

[2]*Southern Methodist University, Dallas, Texas, USA*

Natural Hazard Uncertainty Assessment: Modeling and Decision Support, Geophysical Monograph 223, First Edition.
Edited by Karin Riley, Peter Webley, and Matthew Thompson.

and accuracy of this technique in geodetic applications. In the studies of earthquake source models by using InSAR-derived observations, previous efforts have been made on assessing the uncertainties and trade-offs of estimated earthquake source parameters, where the simulated interferograms with realistic noise levels have been generated and inverted [e.g., *Dawson and Tregoning*, 2007; *Lohman and Simons*, 2005]. Even though InSAR has been widely used to estimate the volcanic source parameters (geometry and volume change), there are limited reports on how InSAR observations could reduce the quality of estimated source parameters. For example, *Lu et al.* [2003] reported that the atmospheric contamination could lead to biased estimates of source depth in studying Westdahl volcano, Alaska, USA.

In this study, we present a systematic study on estimating uncertainties associated with volcano source parameters from InSAR observations, through the simulated interferometric data and the inversion of Mogi source model [*Mogi*, 1958]. The Mogi model is selected because of its capability in approximating volcano sources, simplicity (hence computational efficiency), and wide use. In the rest of this paper, we will present a section on uncertainties related to InSAR-measured volcano deformation, and a brief introduction to the analytical Mogi source model. The inherent impacts from InSAR measurement uncertainties on the estimated volcano source model parameters will be investigated quantitatively. Finally, a brief discussion is provided regarding the impacts of the assumptions in Mogi source model on the estimated source parameters.

7.2. VOLCANO DEFORMATION FROM INSAR AND THE ASSOCIATED UNCERTAINTIES

7.2.1. Uncertainties in InSAR Observations

Interferometric SAR (InSAR) involves the use of two or more synthetic aperture radar (SAR) phase images of the same area to generate interferograms [*Burgmann et al.*, 2000; *Lu and Dzurisin*, 2014; *Massonnet and Feigl*, 1998; *Rosen et al.*, 2000; *Simons and Rosen*, 2007]. The phase component of a SAR image is controlled mainly by the round-trip travel time from SAR to ground. Hence, the interferogram (i.e., the phase difference of SAR images) along with a digital elevation model (DEM) can be used to extract any surface deformation that might have occurred during the interval between image acquisitions and resulted in a change of distance between satellite and ground. InSAR has been proven an important observational tool for measuring volcano-wide deformation at a spatial resolution of tens of meters with centimeter-level accuracy [e.g., *Amelung et al.*, 2000; *Biggs et al.*, 2010; *Dzurisin et al.*, 2006; *Lu et al.*, 2000, 2005, 2010; *Lu and Dzurisin*, 2014; *Massonnet and Feigl*, 1998; *Poland et al.*, 2006; *Pritchard and Simons*, 2002; *Wicks et al.*, 1998, 2002, 2006].

Uncertainties in our knowledge of the satellite position can cause baseline-induced phase ramps in an interferogram. In addition, the radar phase measurement is also affected by atmospheric conditions (water vapor in the troposphere and electron density in the ionosphere) and by the interaction of the radar signal with the ground surface; therefore, an InSAR image can contain spurious phase anomalies due to atmospheric artifacts and decorrelation noise. These errors should be modeled and removed as much as possible to minimize uncertainties in deformation source parameters.

To mitigate phase ramps as well as topography-dependent phase artifacts related to uncertainties in the SAR antenna positions at the times of image acquisitions (ϕ_{orb}) [e.g., *Lu and Dzurisin*, 2014], baseline refinement steps are often employed. A commonly used method is to determine the baseline vector based on an existing DEM via a least-squares approach [*Rosen et al.*, 1996]. For this method, areas of the interferogram that are used to refine the baseline should have negligible deformation or deformation that is well characterized by an independent data source. Because baseline-induced anomalies are characterized by primarily long-wavelength ramping fringes, they are alternatively often modeled and removed using two-dimensional polynomial functions [*Biggs et al.*, 2007].

Inhomogeneity in the atmosphere that results in path anomalies (ϕ_{aps}) in InSAR phase images is the most significant error source in repeat-pass InSAR deformation measurements. Differences in tropospheric water-vapor content as well as ionospheric variations at two observation times can cause differing path delays and consequent anomalies in an InSAR deformation image. The tropospheric artifact can be classified into two types [*Hanssen*, 2011]: (1) stratified artifact, which is caused by changes in vertical refractivity profile at two image acquisition times, is correlated to the local topography; and (2) turbulent effect, which is caused by three-dimensional heterogeneity in the tropospheric refractivity at image acquisition times, impacts both flat and mountainous areas. Atmospheric delay anomalies can reduce the accuracy of InSAR-derived deformation measurements from several millimeters under ideal conditions to a few centimeters under more typical conditions, thus obscuring subtle changes that could hold clues to the cause of the deformation [e.g., *Lu and Dzurisin*, 2014]. Generally speaking, atmospheric artifacts have shorter spatial wavelength than those due to baselines. The difficulty with estimating water-vapor or ionosphere conditions with the needed

accuracy and spatial density is an important limiting factor in deformation monitoring with InSAR. Several methods have been proposed to estimate the water-vapor content and remove its effect from deformation interferograms:

1. The first method is to estimate water-vapor concentrations in the target area at the times of SAR image acquisitions using short-term predictions from weather models [*Foster et al.*, 2006; *Gong et al.*, 2014; *Jolivet et al.*, 2014]. While weather models would be sufficient to correct stratified atmospheric artifacts over a volcano [*Cong and Eineder*, 2012], the problem with this approach is that current weather models have much coarser resolution (a few kilometers) than InSAR measurements (tens of meters). This deficiency can be remedied to some extent by integrating weather models with high-resolution atmospheric measurements, but this approach requires intensive computation.

2. The second method is to estimate water-vapor concentration from continuous global positioning system (CGPS) observations in the target area [*Li et al.*, 2005]. The spatial resolution (i.e., station spacing) of local or regional CGPS networks at volcanoes is typically a few kilometers to tens of kilometers, which renders this method ineffective in most cases.

3. The third approach to correcting atmospheric delay anomalies in InSAR observations is to utilize water-vapor measurements from optical satellite sensors such as the Moderate Resolution Imaging Spectroradiometer (MODIS), Advanced Spaceborne Thermal Emission and Reflection Radiometer (ASTER), and European Medium Resolution Imaging Spectrometer (MERIS) [*Li et al.*, 2003]. The disadvantage of this method is the requirement of nearly simultaneous acquisitions of SAR and cloud-free optical images.

4. The fourth method extracts the atmospheric contributions from interferometric phases themselves, including many approaches for mitigating ionospheric artifacts, for example, split-spectrum, Faraday rotation related method [*Meyer and Nicoll*, 2008], azimuth offset method, and multiple-aperture interferometry [*Jung et al.*, 2013]. Additionally, methods that account for the correlation between atmospheric delays and the local topography [*Bejar-Pizarro et al.*, 2013], as well as the spatial variability [*Bekaert et al.*, 2015; *Lin et al.*, 2010] can be used to correct stratified atmospheric delays. However, those solutions have limited impacts on reducing turbulent mixing tropospheric component.

5. The fifth technique is to correct atmospheric delay anomalies using a multi-temporal InSAR technique [e.g., *Berardino et al.*, 2002; *Ferretti et al.*, 2001; *Hooper et al.*, 2007; *Lu and Dzurisin*, 2014]. When more than several SAR images are available for a given study area, multi-interferogram InSAR processing can be employed to improve the accuracy of deformation maps. If there is sufficient knowledge on the deformation behavior, a temporal deformation model can be built and used to constrain the atmospheric phase mitigation. Otherwise, atmospheric artifacts can be removed via spatial-temporal filtering processes, as they are characterized as spatially correlated but temporally uncorrelated fringes while deformation signals are correlated in both space and time domains. This technique is most promising when a large SAR stack is available, because more SAR observations allow better characterization of the spatial-temporal properties of different interferometric phase components.

The accuracy of interferometric phase is also affected by decorrelation noise (ϕ_{decor}), including the temporal, geometric, and volumetric decorrelation as well as other radar receiver noise [*Hanssen*, 2001; *Lu and Dzurisin*, 2014]. In volcano studies, decorrelation is aggravated by surface changes related to volcanic eruptions (lava and lahar flows, ashfall), seasonal or perennial changes of snow and ice in high-latitude regions, dense vegetation in middle to lower regions, and layover or shadowing effects under complex terrain conditions. In a typical scenario, the region around a volcano's summit loses coherence. Several examples from C-band data are given in Figure 7.1. These examples show than the volcanic summits often lose coherence even if only summer images separated by one satellite revisiting cycle are used. Decorrelation over the volcano peaks, where volcanic deformation is expected to be largest, can compromise the accuracy of source parameters estimated from InSAR data.

An InSAR image might also contain errors due to inaccurate DEMs (ϕ_{topo}). Despite the increasing availability of remote-sensing-derived DEM data, this is a continuous issue at active volcanoes, as their topography is constantly modified by eruptive activity. The availability of TanDEM DEM [*Krieger et al.*, 2007], newly released enhanced 1-arc-second SRTM DEM [*SRTM*, 2015], and tandem ERS-1/ERS-2 images [e.g., *Lu et al.*, 2011] can reduce this error source. Additionally, if multiple SAR images are available over a study area, the existing DEM can be updated or refined using interferograms with large spatial baselines but short temporal separations [e.g., *Lu et al.*, 2013; *Lu and Dzurisin*, 2014]. This scheme of baseline setting is used to reduce impacts from the deformation signal and other phase artifacts on the DEM as large spatial-baseline interferograms are more sensitive to the ϕ_{topo} and the small temporal-baseline reduces the contamination by the deformation signal. The non-topography-related signals can be further mitigated based on temporal-spatial statistical properties of different phase components (e.g., reduce atmospheric signal

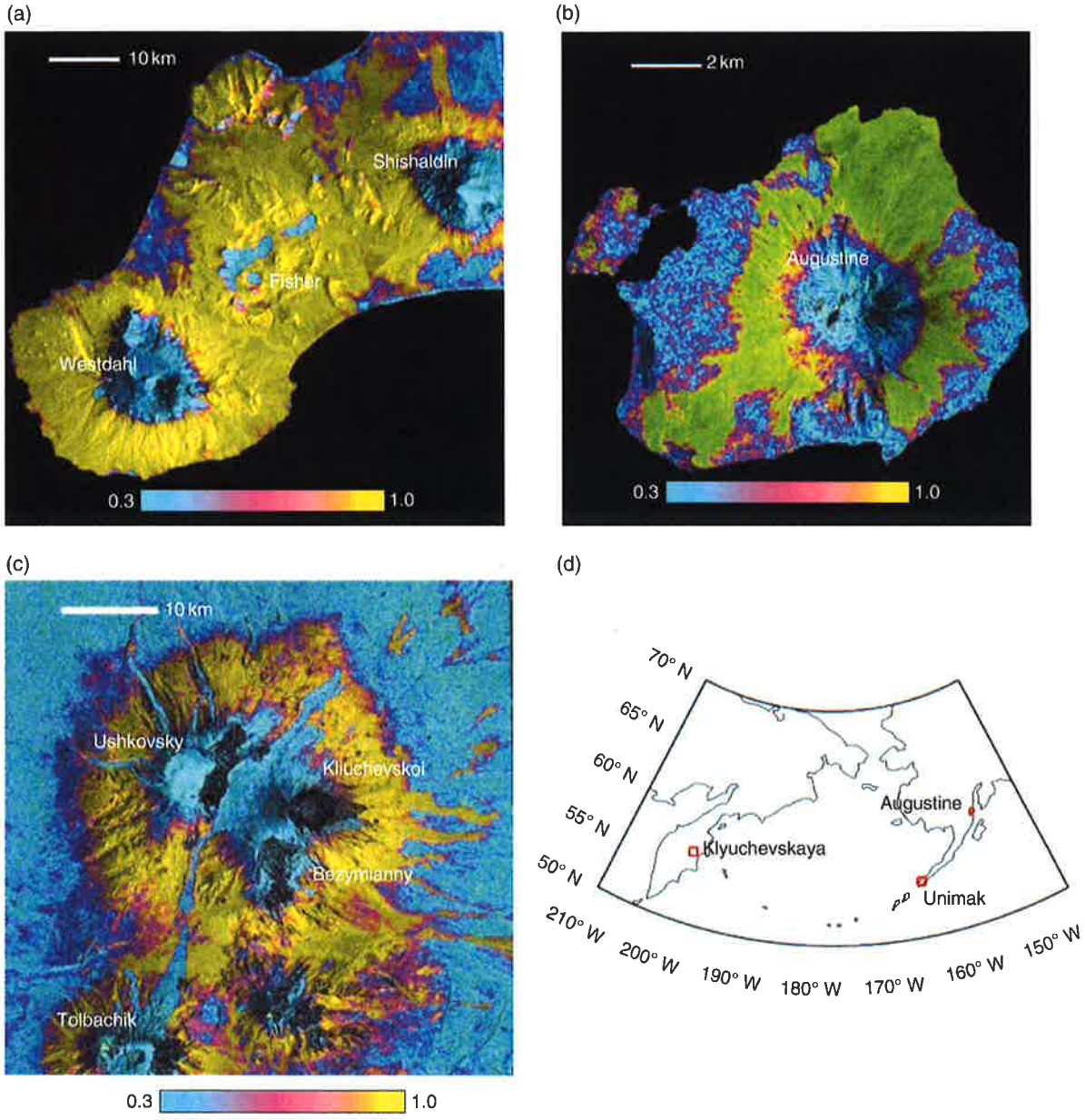

Figure 7.1 Coherence image examples of volcanoes in high-latitude region during summer to early fall. Coherence images are overlaying on the corresponding radar intensity images and major volcanoes in the example sites are annotated: (a) Envisat data pair of Unimak Island (Alaska, USA) with a 35-day time interval, (b) Radarsat-1 data pair of Augustine volcano (Alaska, USA) with a 24-day time interval, (c) Envisat data pair of Klyuchevskaya group of volcanos (Kamchatka, Russia) with a 35-day time interval, (d) geographic locations of the coherence images shown in (a), (b), and (c).

through stacking). Errors of the inaccurate DEM, which is a function of ϕ_{topo} and perpendicular baseline, is then estimated.

Finally, for volcano studies, regional tectonic signals or other geophysical signals might introduce long wavelength "artifacts" (ϕ_{artf}) on volcano-wide deformation, for example, ocean tidal loading that may however have only small influence on volcano studies (e.g., 3 cm over 100 km [*DiCaprio and Simons*, 2008]). Often, this type of long wavelength signal can be confused with baseline errors [*Zhang et al.*, 2014] and is likely removed along with the phase ramp due to baseline error.

Both ϕ_{topo} and ϕ_{orb} are considered as deterministic errors, which are error terms that can be modeled explicitly [*Hanssen*, 2001]. They can be removed in the deformation phase reconstruction step or jointly be estimated in the geophysical model inversion. For example, ϕ_{orb} is modeled as ramps and integrated in volcano and earthquake model inversions [*Gong et al.*, 2014; *Lu et al.*, 2010; *Sudhaus and Jonsson*, 2009]. The remaining error terms, mainly ϕ_{aps} and ϕ_{decor}, are typically considered in the stochastic model that contributes to the variance-covariance matrix (or noise model) of the measurements [*Hanssen*, 2001]. Previous efforts have been made to explicitly integrate these error sources in the InSAR noise model [e.g., *Hanssen*, 2001; *Knospe and Jonsson*, 2010; *Lohman and Simons*, 2005], such that each pixel can be properly weighted in the geophysical parameter inversion and uncertainties of estimated model parameters can be predicted.

7.2.2. Satellite Line-of-Sight Measurements

The error characteristics of geophysical parameters derived from InSAR are additionally impacted by the oblique imaging geometry of SAR sensors, which limits the measurement sensitivity of InSAR to the projection of the three-dimensional deformation signal is in the sensor's line-of-sight (LOS) direction. Using the notation by *Wright et al.* [2004] and *Lu and Dzurisin* [2014], the deformation signal for ground pixel i in east, north, and up directions ($[d_{i,e},\ d_{i,n},\ d_{i,u}]$) is projected into the sensor's LOS direction by multiplying by the unit vector $\Lambda = [-cos\phi \cdot sin\theta,\ \sin\phi \cdot sin\theta,\ cos\theta]$, where θ is the incidence angle and ϕ is the satellite track angle clockwise from north.

$$d_{i,los} = \Lambda \cdot \left[d_{i,e},\ d_{i,n},\ d_{i,u}\right]^T \tag{7.1}$$

In equation (7.1), $d_{i,los}$, $d_{i,e}$, $d_{i,n}$, and $d_{i,u}$ are deformation measurements in the LOS, east, north, and up directions in the ith interferogram, respectively. Thus, an interferogram provides a scalar one-dimensional deformation measurement at every coherent pixel. When interferograms in multiple geometries are available, one can solve equation (7.1) to derive the 3-D deformations. However, it is difficult to resolve the displacements in N-S direction with the near-polar orbiting satellite data in general [*Wright et al.*, 2004]. The offset tracking method or multiple aperture InSAR (MAI) can be used to extract the along-track displacement under favorable conditions [*Bechor and Zebker*, 2006; *Jung et al.*, 2011].

7.3. RETRIEVAL OF MAGMA SOURCE PARAMETERS FROM INSAR AND ASSOCIATED MEASUREMENT UNCERTAINTIES

7.3.1. Mogi Source

To better understand volcanic processes, mathematical models are often employed to relate the physical parameters of a magma source to the deformation measurements made at the surface (e.g., via InSAR or GPS). The high spatial resolution and large spatial extent of surface deformation data provided by InSAR make it possible to constrain and compare models with various source geometries and gain insight into the most likely shape, location, and volume change within a volcanic source. Typical source geometries include the point pressure source [*Mogi*, 1958], finite spherical source [*Mctigue*, 1987], dislocation sources (sill or dike source) [*Okada*, 1985], ellipsoidal sources [*Davis*, 1986; *Yang et al.*, 1988], and penny-crack sources [*Fialko et al.*, 2001]. Among the physical parameters, the location and volume change of the source are usually of most interest.

The most widely used source in volcano deformation modeling is the point pressure source (widely referred to as the Mogi source) embedded in an elastic homogeneous half-space [*Mogi*, 1958]. In a Cartesian coordinate system, the predicted displacement u at the free surface due to a change in volume ΔV or pressure ΔP of an embedded Mogi sphere is:

$$\begin{aligned} u_i\left(x_1 - x_1', x_2 - x_2', -x_3\right) &= \Delta P(1-\nu)\frac{r_s^3}{G}\frac{x_i - x_i'}{\left|R^3\right|} \\ &= \Delta V \frac{(1-\nu)}{\pi}\frac{x_i - x_i'}{\left|R^3\right|} \end{aligned} \tag{7.2}$$

where x_1', x_2', and x_3' are the horizontal coordinates and depth of the center of the sphere, R is the distance between the center of the sphere and the observation point (x_1, x_2, and 0), ΔP and ΔV are the pressure and volume changes in the sphere, and ν is Poisson's ratio of the host rock (typical value is 0.25). Furthermore, r_s is the radius of the sphere, and G is the shear modulus of the host rock [*Delaney and Mctigue*, 1994; *Johnson*, 1987].

7.3.2. Nonlinear Least-Squares Estimation of Mogi Source Parameters

The determination of the Mogi source geometry and volume change from InSAR deformation measurements is a typical nonlinear inverse problem. The problem can be solved by a nonlinear optimization that searches for the optimal source model parameters by minimizing a

misfit function. The misfit (S) describes the level of disagreement between the observed deformation ($d_{i,obs}$) and the source model prediction [*Cervelli et al.*, 2001; *Lu and Dzurisin*, 2014] that accounts for unmolded residuals, including InSAR measurement errors and impacts from oversimplifications in the source model (e.g., elastic half-space), among others. Equation (7.3) shows the minimum misfit constraint in the residual variance:

$$S_{\min} = \arg\min \frac{\Sigma\left(\Lambda \cdot u_i(X') - d_{i,obs}\right)^2}{N-p} \tag{7.3}$$

in which N is the number of coherent pixels in an InSAR image and p is the number of unknowns in the analytical volcano source model; X' is the vector of the source geometry (x_1', x_2', and x_3').

Various strategies are available to solve the inverse problem by finding global minima (e.g., simulated annealing) and/or local minima (e.g., nonlinear least-squares schemes) [*Cervelli et al.*, 2001; *Feigl et al.*, 1995; *Lu and Dzurisin*, 2014; *Press et al.*, 2007; *Sudhaus and Jonsson*, 2009; *Wright et al.*, 1999]. The benefit of global minima algorithms is the ability to discriminate among multiple local minima in the solution space [*Mosegaard and Tarantola*, 1995]. Otherwise, with a reasonable initial guess of model parameters, the nonlinear least-squares algorithms can be used [*Cervelli et al.*, 2001; *Feigl et al.*, 1995], which is computationally more efficient. In the rest of this paper, the Levenberg-Marquardt algorithm, a nonlinear least-squares algorithm that optimizes the solution between iterative linearization and gradient methods [*Marquardt*, 1963; *Press et al.*, 2007], is used to solve for the inversion of Mogi source parameters with InSAR data.

7.3.3. Deriving Uncertainty Measures for Estimated Mogi Model Parameters

After the source geometry and associated volume change are determined, the next goal is to assess the quality of estimated parameters. Thus, we need to find the associated uncertainties (or confidence level, posterior probability distribution) of model parameters. In this section, we will discuss impacts on uncertainties (posterior probability estimates) due to measurement errors. Synthetic deformation interferograms are generated from a predefined Mogi source and then converted to radar's LOS geometry and a coherence map of Westdahl volcano (Fig. 7.1a) is used to approximate realistic coherence conditions for complex volcanic terrains.

There are various methods that can be used to propagate observational errors to the estimate parameters, for example, linearization, likelihood, Monte Carlo simulation, and bootstrap [*Donaldson and Schnabel*, 1987; *Draper and Smith*, 1966; *Press et al.*, 2007]. A linearization method calculates the uncertainties of estimated parameters with the estimated residual variance $S' = \frac{\Sigma(\Lambda \cdot u_i(X') - d_{i,obs})^2}{N'-p}$ [*Donaldson and Schnabel*, 1987]. Notice that N' is the number of independent deformation measurements. For instance, the parameter variance-covariance matrix can be computed with Jacobian matrix (J) as $S'(J^T \cdot J)^{-1}$. However, due to the dependency of InSAR deformation measurements, N' is generally less than N. Without a properly determined N', the linearization method will underestimate the uncertainties of estimated parameters. The advantage of the linearization method is that it is less computationally intensive.

The Monte Carlo simulation and the bootstrap methods, which can be performed with less computational efficiency, have been suggested to be more reliable in constructing the confidence intervals of the estimated parameters [*Arnadottir and Segall*, 1994; *Donaldson and Schnabel*, 1987]. The bootstrap method can be applied without sufficient knowledge of the measurement error, while special attention is needed to draw random samples to satisfy the statistical preassumption [*Lisowski*, 2007; *Press et al.*, 2007]. Additionally, there has been overestimation reported on confidence intervals when using the bootstrap method [*Cervelli et al.*, 2001]. When prior information or valid assumptions about the statistical properties of the measurement errors are available, the Monte Carlo method is supposed to correctly characterize the error properties of the estimated parameters [*Donaldson and Schnabel*, 1987; *Press et al.*, 2007]. The Monte Carlo method has been implemented in many geodetic studies to determine the posterior probability distribution of volcanic or earthquake model parameters [*Feigl et al.*, 1995; *Hooper et al.*, 2007; *Wright et al.*, 2003]. In order to provide accurate results on source model parameter uncertainties, we generate simulated error-contaminated unwrapped interferograms so that statistical properties of InSAR residuals are known and have been set up to approximate the reality conditions. Taking the advantage of the known InSAR error properties and stable performance of Monte Carlo method in providing reliable results, we choose the Monte Carlo method in our study to derive uncertainties of the estimated source model parameters.

7.3.3.1. Summary of Main InSAR Measurement Errors and Error Propagation Approach

Summing up the errors discussed in Section 7.2.1, the main contribution of InSAR deformation phase residuals ϵ is shown in equation (7.4).

$$\epsilon = \phi - \phi_{defo} = \phi_{aps} + \phi_{orb} + \phi_{topo} + \phi_{decor} \quad (7.4)$$

According to the spatial properties of above error components, ϵ can be categorized into three groups: (1) spatial uncorrelated error (ϵ^u) that contributes to diagonal elements (variance) of measurements' variance-covariance matrix. The variance characterizes the quality of the single point and can be predicted or estimated from coherence condition (ϕ_{decor}) [*Hanssen*, 2001]; (2) locally correlated errors (ϵ^a) that are mainly caused by localized atmospheric structures (ϕ^s_{aps}), which are correlated within a few kilometers [*Colesanti et al.*, 2003]; and (3) long-wavelength errors ϵ^l, which include long-wavelength atmospheric signal components ϕ^l_{aps} and ϕ_{orb} [*Biggs et al.*, 2007]. ϕ_{topo} is related to the accuracy of external terrain model; this term will not be considered here as this deterministic term can be removed when interferograms of different baselines are available. Additionally, topography-related atmospheric signal will also not be discussed in the following part, given it can be modeled and reduced via many previous discussed methods (see Section 7.2.1). Overall, both ϵ^a and ϵ^l create spatial correlations among InSAR pixels that leads to nonzero covariance and affect model parameter confidence intervals [*Hanssen*, 2001; *Lohman and Simons*, 2005].

To conduct our error analysis, we start with a simulated surface inflation data set corresponding to a Mogi-type volcanic source with source geometry of $x_1' = 21\text{km}$, $x_2' = 16$, $x_3' = 6\text{km}$ in local coordinates and $\Delta V = 10 \times 10^6\ \text{m}^3$. The lower-left corner is defined as the origin of the local coordinate used in the inversion. For every error type, we use Monte Carlo simulation techniques to create a sufficient number of simulated phase screens that are representative for the individual error type. We add these phase screens to the simulated Mogi-type deformation map to create a random sample of distorted InSAR data. For every simulated phase map, we apply the previously mentioned nonlinear least-squares inversion with the same initial bounds to estimate Mogi source parameters. The posterior probability distributions for these parameters can then be generated and analyzed according to input InSAR error types and mean values of distributions are expected to approximate the true Mogi source parameters.

7.3.3.2. Effects of ϵ^u, ϵ^a, and ϵ^l on the Accuracy of Source Model Parameters

The approaches to generate random realizations of the three different error types together with the resulting posterior distributions for the four Mogi model parameters are summarized in the following:

1. The spatially uncorrelated errors (ϵ^u) are simulated as normally distributed random signals and added to true deformation maps. The standard deviation (σ) of ϵ^u (one way error contribution) in the individual interferogram ranges from about 2 to 10 mm with median value of about 6 mm. An example of InSAR deformation map with ϵ^u is given in Figure 7.2b where the noise σ is about 6 mm. Assuming the analyzed interferometric targets are single-looked distributed scatterers, their phase variances can be predicted from the magnitude of complex coherence (γ) and Euler's dilogarithm [*Bamler and Hartl*, 1998]. Hence, a phase noise σ of 6 mm corresponds to an unfiltered coherence level of above 0.5 in case of C-band data. The posterior probability distribution of estimated parameters due to ϵ^u error conditions are approximately normally distributed for all four Mogi source parameters (Fig. 7.3). The confidence intervals at 95% confidence level (2σ) are shown as red lines in Figure 7.3 and the standard deviations and mean values of the posterior distribution are listed in Table 7.1. Figure 7.3 shows that the addition of random noise does not lead to significant biases of the estimated parameters.

To further analyze the influence of random errors, we increase the noise level of ϵ^u to $6mm < \sigma < 14mm$ with median value of about 10 mm that might correspond to severe decorrelation of distributed targets in C-band interferograms. For this setup, the standard deviations of the posterior distributions increase (see Table 7.1) but still maintain normal distribution with mean values that are statistically identical to their true values (at the 95% confidence level).

2. The locally correlated errors (ϵ^a), which are dominated by local scale atmospheric distortions [*Emardson et al.*, 2003; *Hanssen*, 2001; *Lohman and Simons*, 2005], are simulated as a set of atmospheric phase screens. The simulated ϵ^a were generated using a fractal surface with a dimension factor of 2.67, which is an typical value for the dimension factor as suggested for the atmospheric signal simulation [*Hanssen*, 2001; *Kampes*, 2006]. The family of ϵ^a used in this experiment has standard deviations of less than 12 mm with a median value of 3.9 mm. This value range has been set to resemble the realistic situation: for example, atmosphere error standard deviation has been reported to be less than 15 mm in southern San Andreas [*Lyons and Sandwell*, 2003], and less than 12 mm in multiple test sites (Mexico City, Netherlands, and South Australia; *Liu* [2012]). An example is given in Figure 7.2c with a noise standard deviation of 3.3 mm. Note that the simulated ϵ^a mainly accounts for the atmosphere turbulence mixing; the standard deviation of the total atmospheric artifact in an interferogram is supposed to be larger, given that the stratification is also included. Similar to the last experiment, through Monte Carlo simulations, we can draw the posterior probably distributions for all estimated parameters (Fig. 7.4). The source parameter's standard deviations are shown in Table 7.2 and range from 1 km to 1.6 km for the positions of the Mogi source.

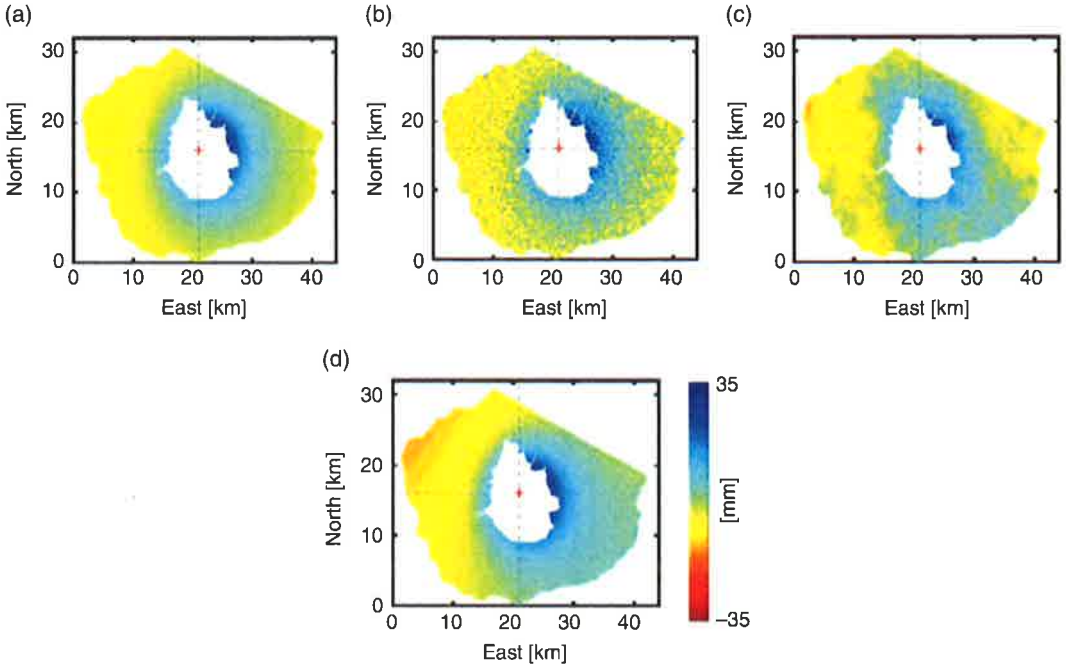

Figure 7.2 Example of one way LOS deformation images in a descending imaging geometry without/with measurement errors. The red marker is the location of Mogi source center. (a) True LOS inflation of Mogi source; (b) deformation contaminated by ϵ^u; (c) deformation contaminated by ϵ^a; (d) deformation contaminated by ϵ^l.

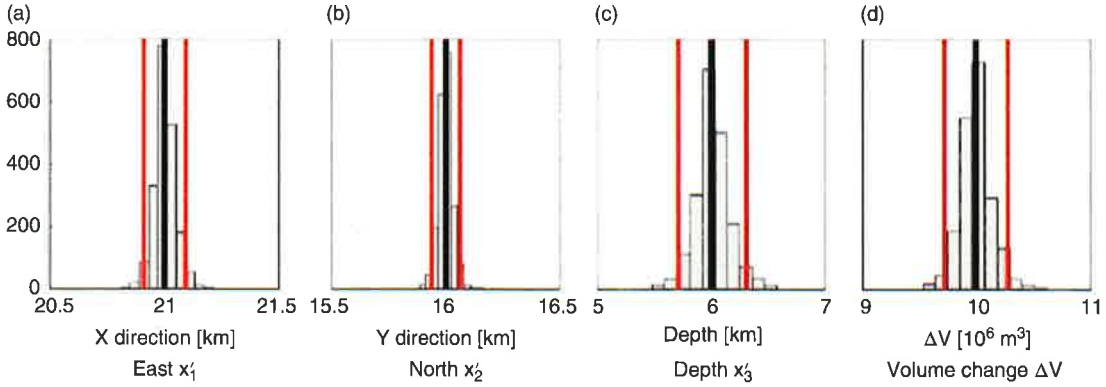

Figure 7.3 Example of probability distribution of estimated parameters where measurements have spatially uncorrelated errors ϵ^u. Red bars denote 2σ confidence bounds and black bars denote the true value of the Mogi source parameters (the same holds for Figures 7.4 and 7.5).

For each of the four parameters, the probability distribution is approximately normal. In Figure 7.4c, the estimated probability distribution of the depth is distorted on the high end by our choice for the initial bounds (2–8 km) of the nonlinear least-squares inversion. While the mean values of x_3' and ΔV differ from the true values, they are still statistically identical to their theoretical values at the 95% confidence level. Given the trade-off between these two parameters [*Mann and Freymueller*, 2003], it was suggested that the ϵ^a errors could cause difficulties in distinguishing these two parameters.

3. The third dataset was generated by simulating long-wavelength errors (ϵ^l) whose shape is approximated by planar phase screens as shown in equation (7.5). These phase screens are used to model both ϕ_{orb} and long-wavelength atmospheric signal components [*Biggs et al.*, 2007; *Lu and Dzurisin*, 2014]. An example is given in Figure 7.2d with noise standard deviation of about 3.3 mm and N-S slope coefficient of 0.26 mm/km and W-E slope coefficient of −0.23 mm/km.

$$\epsilon^l = a \cdot x_1 + b \cdot x_2 + c \tag{7.5}$$

Table 7.1 Mean and Standard Deviation (σ) of Estimated Mogi Source Parameters With ϵ^u Errors in Deformation Measurements

		x_1' [km]	x_2' [km]	x_3' [km]	$\Delta V \times 10^6$ m^3
Lower	Mean	21.00	16.00	6.01	10.00
ϵ^u	σ	0.05	0 .03	0.15	0.14
Higher	Mean	21.00	16.00	6.02	10.00
ϵ^u	σ	0.07	0.05	0.23	0.22

Note: The true values of source parameters are $x_1' = 21$ km, $x_2' = 16$ km, $x_3' = 6$ km, and $\Delta V = 10 \times 10^6$ m^3.

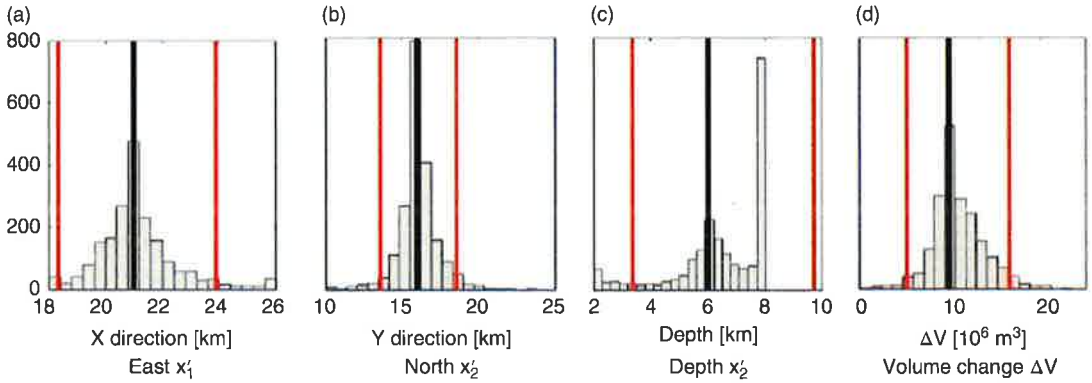

Figure 7.4 Probability distribution of estimated parameters when measurements have spatially correlated errors ϵ^a.

Table 7.2 Mean and Standard Deviation (σ) of Estimated Mogi Source Parameters When the Deformation Measurement Contains ϵ^a and ϵ^l, Respectively

		x_1' [km]	x_2' [km]	x_3' [km]	$\Delta V \times 10^6$ m^3
ϵ^a	Mean	21.12	16.06	6.53	10.97
	σ	1.39	1.23	1.59	2.82
ϵ_1^l	Mean	20.99	15.91	7.81	12.58
	σ	2.09	2.69	0.58	3.60
ϵ_2^l	Mean	21.09	16.00	7.39	11.59
	σ	1.27	1.40	0.90	2.41

Note: The true values of source parameters are $x_1' = 21$ km, $x_2' = 16$ km, $x_3' = 6$ km, and $\Delta V = 10 \times 10^6$ m^3.

The parameters $[x_1, x_2]$ in equation (7.5) are the local coordinates of a pixel in the synthetic datasets, while a and b are the simulated east-west and north-south slope coefficients, and c is the intercept. *Biggs et al.* [2007] has found that for typical ERS-type SAR interferograms, long-wavelength phase ramps have slope coefficients that are roughly normal distributed, centered to zero, and with absolute values of smaller than 2 mm/km. Based on these empirical results, we use Monte Carlo simulation to create a family of phase screens ϵ_1^l with slope coefficients whose statistical properties resemble the observations in the study by *Biggs et al.* [2007]. The phase screens were added to the deformation data and a nonlinear least-squares inversion was used to estimate the Mogi model parameters from the distorted data. The inversion results are shown in Table 7.2, indicating that the performance on x_3' and ΔV estimation is poor. With this level (ϵ_1^l) of long-wavelength errors, the trade-off between depth and volume change intensively hampers the parameter estimation.

Thus, we reduce long wavelength noise level (ϵ_2^l) to a set of smaller slope coefficients (within $[-1, 1]$ mm/km) in both directions, by assuming that most of the ramp signals can be compensated using preprocessing procedures. The posterior probability distributions obtained based on these reduced long-wavelength noise levels (ϵ_2^l) are shown in Figure 7.5 and their statistics are listed in Table 7.2. The

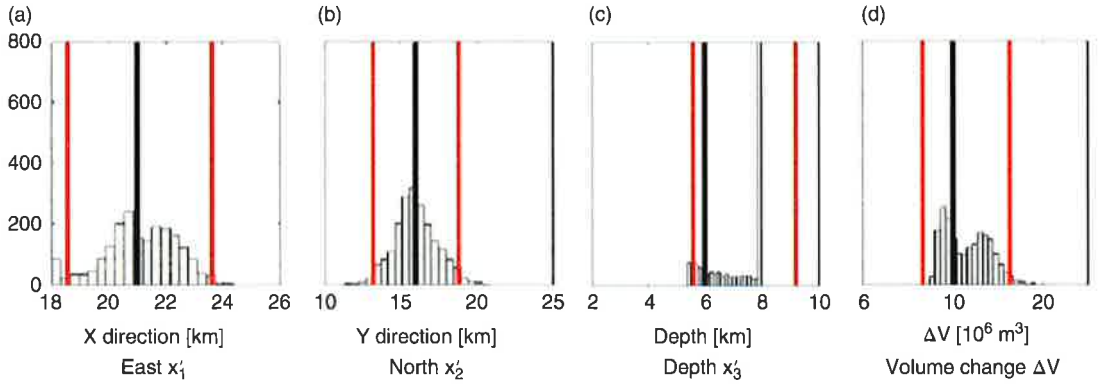

Figure 7.5 Probability distribution of estimated parameters when measurements have spatially local correlated errors ϵ^l.

source depth and volume change still appear to be poorly constrained in this case and the histogram of ΔV is bimodal. The spatial standard deviation of ϵ_2^l and ϵ^a in the last case study are within the same value range (less than 12 mm) yielding similar uncertainties of the estimated Mogi parameters (e.g., $1-\sigma$ uncertainties of source horizontal location is about 1–1.5 km). However, the posterior probability distributions, especially for x_3' and ΔV, are less normal for data affected by long-wavelength errors. For x_3' and ΔV, the mean values of the estimated source parameters differ from their theoretical values but this difference remains statistically insignificant (at the 95% confidence level).

Overall, from our experiments, we can draw the following conclusions for the dependence of the posterior probabilities of the estimated Mogi source parameters on different phase noise types:

1. Spatially correlated noise (ϵ^l and ϵ^a) can significantly impact the accuracy with which the parameters of a volcanic source model can be determined. Strongest impacts are observed for the accuracy of source depth and volume change. In comparison, the influence of ϵ^a on the estimated model parameters is small.

2. InSAR deformation maps containing ϵ^l and ϵ^a errors reduce our ability to determine source depth and volume change parameters. Here, especially long wavelength ϵ^l errors are harmful.

3. Reducing ϵ^l and ϵ^a errors prior to source model inversion is highly recommended; alternatively, ϵ^l could also be jointly modeled in the inversion.

7.3.3.3. Estimation Errors Related to the Flat-Surface Assumption

Many volcanic inflation/deflation analytical source models (including the Mogi model) apply a flat-surface assumption, that is, they ignore the local topography of the area of interest and assume that all measurement points are located at the same level. Some researchers have suggested that ignoring the local surface topography may lead to biases in the estimated model parameters [*Cayol and Cornet*, 1998; *Williams and Wadge*, 1998]. Correction methods have been proposed that use simple first-order approximations of the topography variation relative to the reference frame or include a higher order correction scheme [*Williams and Wadge*, 1998; 2000]. Simply speaking, neglecting local surface topography will lead to increased misfits in the parameter inversion.

To analyze the impact of ignoring surface topography, we first compute and compare surface deformation signals caused by an inflating Mogi source for (1) a model that uses the flat-surface assumption (u_f) and (2) a situation where the local topography is considered when evaluating the Mogi forward model in equation (7.2) (u_T).The topography of Westdahl volcano is used as an example in this study and full coherence is assumed (Fig. 7.6). These results indicate that ignoring local topography can lead to significant overestimation of displacement, especially in areas near the center of the volcano where effects caused by ignoring topography in modeling are the largest. The overestimation is caused by the fact that the distance between the source location and the measurement points is underestimated if surface topography is ignored. Errors are generally smaller on the flank farther away from source center. Generally, the effect of the flat-surface assumption depends on the ratio of topographic height to source depth. The deeper the source and, hence, the smaller this ratio, the smaller the error introduced by ignoring topography. Overall, comparing Figure 7.6(a) and (b) suggests that residuals from $(u_T - u_f)$ are a function of height and distance from the volcano source center. For example, the highest peak that locates north of the source center contains relatively small residual. It also explains the widespread residual values with increasing height as shown in Figure 7.6(c). Note that pixels with larger errors are located around the volcano peak where InSAR coherence is generally lost in real data application, as discussed earlier.

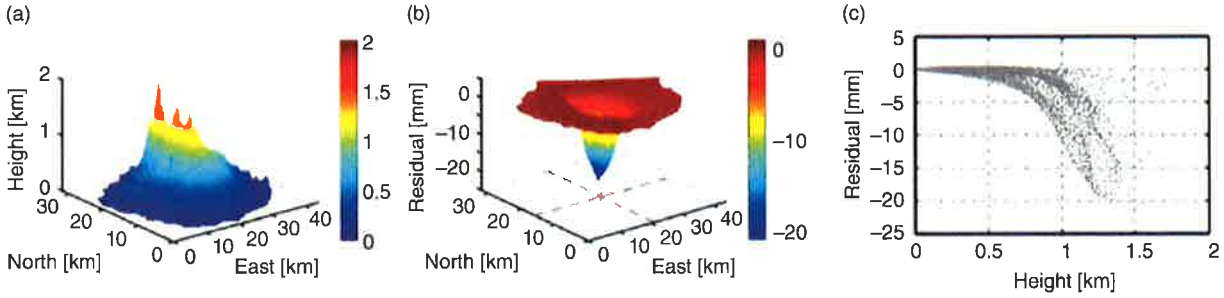

Figure 7.6 Predicted LOS displacements for flat-surface Mogi model (u_f) and elevation-varying Mogi model (u_T): (a) 3D view of the terrain condition of test site, and (b) the spatial distribution of residual displacements of $u_T - u_f$ in millimeters. The red cross indicates the horizontal location of the source center. (c) The relation between the residual of $u_T - u_f$ and the local topography.

Table 7.3 Biased Estimation From Flat-Surface Assumption in Mogi Model

	x_1' [km]	x_2' [km]	x_3' [km]	$\Delta V \times 10^6$ m^3
Coherence everywhere	21.48	15.88	7.16	10.51
Decorrelation	21.14	15.92	6.45	10.10

Note: The true values of source parameters are x_1' =21 km, x_2' =16 km, x_3' =6 km, and ΔV=10 $\times 10^6$ m^3.

To further investigate how the flat-surface assumption affects the source parameter estimation process, we generate two LOS displacement maps for two different coherence conditions, one where full coherence is considered and one where we assume decorrelation near the summit area (see previous examples for the shape and size of the decorrelated area). These LOS deformation maps are prepared while fully considering surface topography resulting in unbiased deformation maps u_T. Finally, to solve for the volcano source parameters, we make the typically used flat-surface assumption in the inversion process. Shown in Table 7.3 are the estimated source parameters compared to their true value (shown in brackets). It can be seen that while biases are introduced to all four model parameters, these biases are most severe for the source depth (x_3') and volume change (ΔV) parameters. It can be seen that biases are larger if coherence near the summit is preserved. Note that this finding is realistic if the source is located roughly underneath the center of the volcano.

7.3.3.4. Joint Inversion with Descending and Ascending Orbit Data

Previous studies have suggested that inversions for an analytical deformation model can be greatly improved if InSAR-based displacement measurements from different geometries are combined in a joint inversion [*Biggs et al.*, 2007; *Lu and Dzurisin*, 2014; *Wright et al.*, 2004]. With sufficient independent measurements, the 3-D deformation map can be reconstructed and then used to constrain the inversion. Alternatively, the vertical and east-west deformations can be derived from interferograms from descending and ascending orbits [*Yun et al.*, 2006].

To discuss how joint inversion would impact the Mogi source parameter estimation, we first perform the nonlinear inversion and Monte Carlo method to compute the posterior probability distribution of source parameters based on synthetic datasets for descending orbit-only (Fig. 7.2a) and ascending orbit-only (Fig. 7.7a) configurations. Phase residuals ϵ, the summation of all InSAR error terms, are included with standard deviation less than 9.5 mm and median values of 4.1 mm. From these inversions, we find that descending-only and ascending-only measurements produce source-model estimates with similar error characteristics (see Table 7.2 for descending-type and Table 7.4 for ascending-type results).

Finally, we add another model run where ascending and descending data are used jointly in the Mogi source parameter inversion. The results show a reduction in the parameter's uncertainties if data from both orbit directions are combined. This performance improvement is particularly large for the horizontal location of the Mogi source. However, when the coherence condition is poor, the inversion results from single tracks and joint tracks still have large uncertainties in the depth and volume change parameters, and also the biases in their mean values remain (x_3' = 6 km and $\Delta V = 10 \times 10^6$ m^3). Our results furthermore show that the benefit of joint ascending and descending data improves if coherence over the source

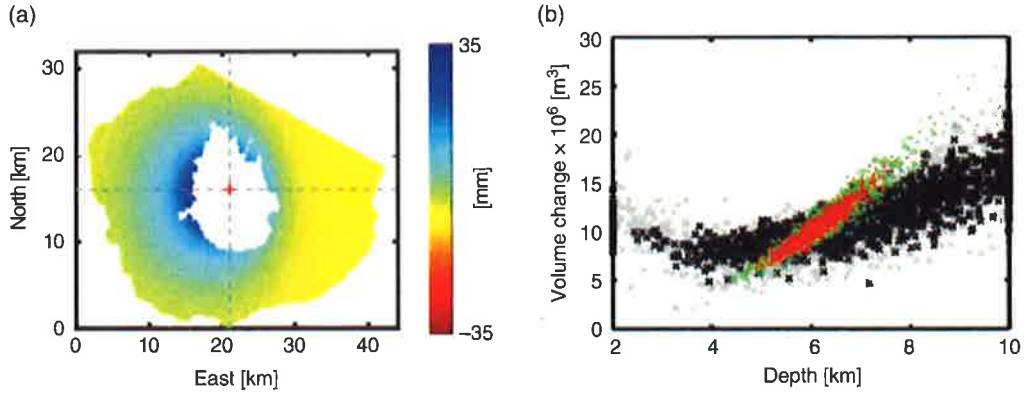

Figure 7.7 An example of Mogi model inversion with descending and ascending track. (a) Synthetic inflation map in ascending geometry; (b) tradeoffs between source depth and volume change. Grey crosses denote the result with ascending orbit data only under poor coherence condition; black crosses denote the result with two orbits under poor coherence condition; green dots denote the result with ascending orbit data only at full coherence; red dots denote the result with two orbits at full coherence.

Table 7.4 Standard Deviation (σ) of Estimated Mogi Source Parameters With Single Track and Multitrack Deformation Maps

			x_1' [km]	x_2' [km]	x_3' [km]	$\Delta V \times 10^6$ m^3
Joint	Decorrelation	mean	21.00	15.99	7.31	12.12
		σ	0.96	0.90	1.96	3.22
	Coherence everywhere	mean	21.00	16.00	6.08	10.30
		σ	0.33	0.31	0.41	1.58
Ascending	Decorrelation	mean	20.86	16.00	7.12	12.13
		σ	1.24	1.18	2.10	4.00
	Coherence everywhere	mean	20.99	16.01	6.16	10.68
		σ	0.44	0.44	0.68	2.60

Note: The true values of source parameters are x_1' =21 km, x_2' =16 km, x_3' =6 km and ΔV=10 ×10^6 m^3.

can be maintained. In this case, biases in source depth and volume change estimates can be reduced.

To further investigate the impact of observation geometry on the separability of x_3' and ΔV we plot the correlation between x_3' and ΔV in Figure 7.7b for different combination of input measurements and coherence conditions. It shows that, as a characteristic of the Mogi model, the trade-off between x_3' and ΔV exists even if observations with full coherence from multiple geometries are available. The results suggest that (1) adding measurements from different look directions will reduce the uncertainties of estimated parameters; (2) if observations are available near the summit (and, hence, above the source location), the uncertainties of source parameters can be reduced. Although we compare only the ascending-only data with the joint-orbit data in this example, the result should be similar if descending-only data were used as long as they possess similar signal-to-noise level and coherence coverage.

7.4. DISCUSSION ON IMPACTS OF OTHER GEOPHYSICAL ASSUMPTIONS ON THE MOGI SOURCE MODEL

Ideally, with accurate ground deformation measurements and adequate inversion strategies, the Mogi source parameters can be well constrained. However, to interpret the estimated volcano source parameters under realistic conditions, the assumptions of the Mogi source model need to be considered (i.e., impacts from the local topography as discussed in the previous section), because they can induce additional uncertainties in the estimated source parameters.

First, the Mogi model has inability to separate pressure change (ΔP) and volume change (ΔV). For instance, the deformation pattern caused by smaller ΔP and larger chamber volume (Vc) cannot be distinguished from that by a combination of larger ΔP and smaller V_c. This is because a point source can be formed by either volume

change (ΔV) as $\frac{\Delta V(1-\upsilon)}{\pi}$ or by the pressure change (ΔP) as $\frac{\Delta P r_S^3}{G(1-\upsilon)}$ as shown in equation (7.2), thus there is $\Delta V = \frac{\Delta P}{G}\pi r_S^3$.

Second, the magma compressibility needs to be considered in understanding the computed volume change from a Mogi model. Notice that the derived ΔV accounts for only the change in the cavity size, which is actually the superposition of injected/withdrawal magma volume (ΔV_m), magma compression (ΔV_c), and volume change of the volatiles [*Johnson*, 1992]. Potentially additional gravitational data and rock physics information would be preferred in order to assist inversion or the interpretation.

Another parameter contributing to the inferred volume change is Poisson's ratio ν. The Mogi model uses an average value of 0.25 for ν, however, the real value of ν depends on the petrological nature of the host-rock and the average ν determined from seismology is considered to be between 0.265 and 0.30 for continental and oceanic crusts [*Christensen*, 1996]. Varying ν has significant impact on the estimated ΔV: the estimated ΔV will increase by 20% if $\nu\nu$ is increased from 0.25 to 0.3 [e.g., *Lu et al.*, 2003]. Thus, it is necessary to consider the uncertainty of volume change due to the usage of an averaged $\nu = 0.25$ in the inversion.

There are also many other assumptions in analytical volcano source models that we will not discuss here (e.g., anisotropic and non-homogeneous expansion environment, inelastic condition of rock [*Masterlark*, 2007]). Hence, we should be aware of the uncertainties from the assumptions used in Mogi model and try not to overinterpret the inversion result.

7.5. CONCLUSION

This chapter presents a study on InSAR measurement uncertainties and inherent impacts on estimated source-model parameters for volcano deformation. The Mogi model is used in the discussion given its simplicity and wide use. Nonlinear least squares and Monte Carlo simulations are used to generate the posterior probability distribution of source parameters. Through experiments with simulated datasets, it suggests that spatially correlated noise is critical to estimate the actual Mogi source parameters and the associated parameter uncertainties. The nonideal coherence condition and existence of spatially correlated InSAR measurement errors emphasize the difficulty in determining the optimal volume change and source depth parameters and their associated uncertainties. The surface topography can impact the estimate of the Mogi source model, thus we suggest a Mogi model with the topography correction incorporated. Adding deformation measurements from different viewing geometry will better constrain the model inversion by reducing uncertainties of estimated parameters.

To interpret the Mogi source parameters for volcano studies in real volcanic conditions, it is important to keep in mind that the computed volume change from geodetic inversion can account for net change of the magma reservoir conceptualized by the Mogi source. Therefore, source model assumptions, for example, the magma compressibility, choice of Poisson's ratio, and volatile concentration, also impact uncertainties of the estimated source volume change. Potentially, together with geological information or/and gravitational data, one can better understand the magma changes in volcano applications.

In this study, we have conducted the tests based on nonlinear inversion with equal weight. However, in the real data analysis, if an adequate InSAR noise model is available, the input deformation maps can be weighted differently so that measurements with large errors will have less impact in the source-model inversion. The InSAR measurements can be weighted using (1) a diagonal variance matrix [e.g., *Wright et al.*, 2004] that only considers the spatially uncorrelated errors, or (2) a more sophisticated full variance-covariance matrix that is formed by also considering the spatial correlation of errors (e.g., building covariance structure by assuming errors are stationary and isotropic [*Lohman and Simons*, 2005]). With a proper weighting scheme, we expect the Mogi source parameter inversion can be better constrained.

ACKNOWLEDGMENTS

Z. Lu acknowledges support from the NASA Earth Surface and Interior Program (NNX14AQ95G) and the Shuler-Foscue Endowment at Southern Methodist University. Constructive comments and reviews from Michael Poland (USGS), Editor-in-Chief Peter Webley, and an anonymous reviewer improved the manuscript.

REFERENCES

Amelung, F., S. Jonsson, H. Zebker, and P. Segall (2000), Widespread uplift and "trapdoor" faulting on Galapagos volcanoes observed with radar interferometry, *Nature*, *407*, 993–996.

Arnadottir, T., and P. Segall (1994), The 1989 Loma-Prieta earthquake imaged from inversion of geodetic data, *J. Geophys. Res. Sol. Earth*, *99*(B11), 21835–21855; doi: 10.1029/94jb01256.

Bamler, R., and P. Hartl (1998), Synthetic aperture radar interferometry, *Inv. Prob.*, *14*, 54; doi:10.1088/0266-5611/14/4/001.

Bechor, N. B. D., and H. A. Zebker (2006), Measuring two-dimensional movements using a single InSAR pair, *Geophys. Res. Lett.*, *33*(16); doi: Artn L1631110.1029/2006gl026883.

Bejar-Pizarro, M., A. Socquet, R. Armijo, D. Carrizo, J. Genrich, and M. Simons (2013), Andean structural control on interseismic coupling in the North Chile subduction zone, *Nat. Geosci.*, *6*(6), 462–467; doi: 10.1038/Ngeo1802.

Bekaert, D. P. S., A. Hooper, and T. J. Wright (2015), A spatially-variable power-law tropospheric correction technique for InSAR data, *J. Geophys. Res. Sol. Earth*, 2014JB011558; doi:10.1002/2014jb011558.

Berardino, P., G. Fornaro, R. Lanari, and E. Sansosti (2002), A new algorithm for surface deformation monitoring based on small baseline differential SAR interferograms, *IEEE Trans. Geosci. Remote Sens.*, *40*(11), 2375–2383; doi: 10.1109/Tgrs.2002.803792.

Biggs, J., T. Wright, Z. Lu, and B. Parsons (2007), Multi-interferogram method for measuring interseismic deformation: Denali fault, Alaska, *Geophys. J. Int.*, *170*(3), 1165–1179; doi: 10.1111/j.1365-246X.2007.03415.x.

Burgmann, R., P. A. Rosen, and E. J. Fielding (2000), Synthetic aperture radar interferometry to measure Earth's surface topography and its deformation, *Ann. Rev. Earth Planet. Sci.*, *28*, 169–209; doi: 10.1146/annurev.earth.28.1.169.

Cayol, V., and F. H. Cornet (1998), Effects of topography on the interpretation of the deformation field of prominent volcanoes: Application to Etna, *Geophys. Res. Lett.*, *25*(11), 1979–1982; doi: 10.1029/98gl51512.

Cervelli, P., M. H. Murray, P. Segall, Y. Aoki, and T. Kato (2001), Estimating source parameters from deformation data, with an application to the March 1997 earthquake swarm off the Izu Peninsula, Japan, *J. Geophys. Res. Sol. Earth*, *106*(B6), 11217–11237; doi: 10.1029/2000jb900399.

Christensen, N. I. (1996), Poisson's ratio and crustal seismology, *J. Geophys. Res. Sol. Earth*, *101*(B2), 3139–3156; doi: 10.1029/95jb03446.

Colesanti, C., A. Ferretti, R. Locatelli, and G. Savio (2003), Multi-platform permanent scatterers analysis: first results, paper presented at Remote Sensing and Data Fusion over Urban Areas, 2003, Second GRSS/ISPRS Joint Workshop on, 22–23 May *2003*.

Cong, X., and M. Eineder (2012), Volcano deformation measurement using persistent scatterer interferometry with atmospheric delay corrections, paper presented at Synthetic Aperture Radar, 2012, EUSAR, Ninth European Conference on 23–26 April 2012.

Davis, P. M. (1986), Surface deformation due to inflation of an arbitrarily oriented triaxial ellipsoidal cavity in an elastic half-space, with reference to Kilauea volcano, Hawaii, *J. Geophys. Res. Solid*, *91*(B7), 7429–7438; doi: 10.1029/Jb091ib07p07429.

Dawson, J., and P. Tregoning (2007), Uncertainty analysis of earthquake source parameters determined from InSAR: A simulation study, *J. Geophys. Res. Sol. Earth*, *112*(B9); doi: 10.1029/2007jb005209.

Delaney, P. T., and D. F. Mctigue (1994), Volume of magma accumulation or withdrawal estimated from surface uplift or subsidence, with application to the 1960 collapse of Kilauea volcano, *B. Volcanol.*, *56*(6–7), 417–424; doi: 10.1007/Bf00302823.

DiCaprio, C. J., and M. Simons (2008), Importance of ocean tidal load corrections for differential InSAR, *Geophys. Res. Lett.*, *35*(22), L22309; doi:10.1029/2008gl035806.

Donaldson, J. R., and R. B. Schnabel (1987), Computational experience with confidence-regions and confidence-intervals for nonlinear least-squares, *Technometrics*, *29*(1), 67–82; doi: 10.2307/1269884.

Draper, N. R., and H. Smith (1966), *Applied regression analysis*, *ix*, Wiley, New York.

Dzurisin, D. (2003), A comprehensive approach to monitoring volcano deformation as a window on the eruption cycle (41), 1001, 2003), *Rev. Geophys.*, *41*(2); doi: 10.1029/2003rg000134.

Dzurisin, D. (2007), *Volcano deformation: Geodetic monitoring techniques*, *xxxv*, Springer-Praxis Berlin; New York; Chichester, UK.

Emardson, T. R., M. Simons, and F. H. Webb (2003), Neutral atmospheric delay in interferometric synthetic aperture radar applications: Statistical description and mitigation, *J. Geophys. Res. Sol. Earth*, *108*(B5); doi: 10.1029/2002jb001781.

Feigl, K. L., A. Sergent, and D. Jacq (1995), Estimation of an earthquake focal mechanism from a satellite radar interferogram - Application to the December 4, 1992 Landers aftershock, *Geophys. Res. Lett.*, *22*(9), 1037–1040; doi: 10.1029/94gl03212.

Ferretti, A., C. Prati, and F. Rocca (2001), Permanent scatterers in SAR interferometry, *IEEE Trans. Geosci. Remote Sens.*, *39*(1), 8–20.

Fialko, Y., Y. Khazan, and M. Simons (2001), Deformation due to a pressurized horizontal circular crack in an elastic half-space, with applications to volcano geodesy, *Geophys. J. Int.*, *146*(1), 181–190; doi: 10.1046/j.1365-246X.2001.00452.x.

Foster, J., B. Brooks, T. Cherubini, C. Shacat, S. Businger, and C. L. Werner (2006), Mitigating atmospheric noise for InSAR using a high resolution weather model, *Geophys. Res. Lett.*, *33*(16); doi: 10.1029/2006gl026781.

Gong, W., F. J. Meyer, C. W. Lee, Z. Lu, and J. Freymueller (2014), Measurement and interpretation of subtle deformation signals at Unimak Island from 2003 to 2010 using Weather Model-Assisted Time Series InSAR, *J. Geophys. Res. Sol. Earth*, 2014JB011384; doi:10.1002/2014jb011384.

GVP (2015), Global Volcanism Program, Smithsonian Institution, http://www.volcano.si.edu/faq.cfm#q3.

Hanssen, R. (2001), *Radar Interferometry: Data Interpretation and Error Analysis*, Kluwer Academic Publishers, Netherlands.

Hooper, A., P. Segall, and H. Zebker (2007), Persistent scatterer interferometric synthetic aperture radar for crustal deformation analysis, with application to Volcán Alcedo, Galápagos, *J. Geophys. Res.*, *112*(B7), B07407; doi:10.1029/2006jb004763.

Johnson, D. J. (1987), Elastic and inelastic magma storage at Kīlauea volcano, in *Volcanism in Hawaii,* edited by Robert W. Decker, Thomas L. Wright, and Peter H. Stauffer, U.S. Geological Survey Professional Paper 1350.

Johnson, D. J. (1992), Dynamics of magma storage in the summit reservoir of Kilauea volcano, Hawaii, *J. Geophys. Res. Sol. Earth*, *97*(B2), 1807–1820; doi: 10.1029/91jb02839.

Jolivet, R., P. S. Agram, N. N. Y. Lin, M. Simons, M. P. Doin, G. Peltzer, and Z. H. Li (2014), Improving InSAR geodesy

using Global Atmospheric Models, *J. Geophys Res. Sol. Earth*, *119*(3), 2324–2341; doi: 10.1002/2013jb010588.

Jung, H. S., D. T. Lee, Z. Lu, and J. S. Won (2013), Ionospheric correction of SAR interferograms by multiple-aperture interferometry, *IEEE Trans. Geosci. Remote Sens.*, *51*(5), 3191–3199; doi: 10.1109/Tgrs.2012.2218660.

Jung, H. S., Z. Lu, J. Won, M. Poland, and A. Miklius (2011), Mapping three-dimensional surface deformation by combining multiple aperture interferometry and conventional interferometry: application to the June 2007 eruption of Kīlauea volcano, Hawaii, *IEEE Geosci. Remote Sens. Lett.*, *8*(1), 34–38.

Kampes, B. (2006), *Radar Interferometry: Persistent Scatterer Technique*, Springer, Dordrecht, Netherlands.

Knospe, S. H. G., and S. Jonsson (2010), Covariance estimation for InSAR surface deformation measurements in the presence of anisotropic atmospheric noise, *IEEE Trans. Geosci. Remote Sens.*, *48*(4), 2057–2065; doi: 10.1109/Tgrs.2009.2033937.

Krieger, G., A. Moreira, H. Fiedler, I. Hajnsek, M. Werner, M. Younis, and M. Zink (2007), TanDEM-X: A satellite formation for high-resolution SAR interferometry, *IEEE Trans. Geosci. Remote Sens.*, *45*(11), 3317–3341; doi: 10.1109/Tgrs.2007.900693.

Li, Z. H., J. P. Muller, and P. Cross (2003), Comparison of precipitable water vapor derived from radiosonde, GPS, and Moderate-Resolution Imaging Spectroradiometer measurements, *J. Geophys. Res. Atmos.*, *108*(D20); doi: 10.1029/2003jd003372.

Li, Z. H., J. P. Muller, P. Cross, and E. J. Fielding (2005), Interferometric synthetic aperture radar (InSAR) atmospheric correction: GPS, moderate resolution imaging spectroradiometer (MODIS), and InSAR integration, *J. Geophys. Res. Sol. Earth*, *110*(B3); doi: 10.1029/2004jb003446.

Lin, Y. N. N. N., M. Simons, E. A. Hetland, P. Muse, and C. DiCaprio (2010), A multiscale approach to estimating topographically correlated propagation delays in radar interferograms, *Geochem. Geophys. Geosysy.*, *11*; doi: 10.1029/2010gc003228.

Lisowski, M. (2007), Analytical volcano deformation source models, in *Volcano Deformation*, 279–304, Springer Praxis, Chichester, UK.

Liu, S. (2012), Satellite Radar Interferometry: Estimation of Atmospheric Delay, Doctoral Dissertation, Delft University of Technology.

Lohman, R. B., and M. Simons (2005), Some thoughts on the use of InSAR data to constrain models of surface deformation: Noise structure and data downsampling, *Geochem. Geophys. Geosyst.*, *6*; doi: 10.1029/2004gc000841.

Lu, Z., and D. Dzurisin (2014), *InSAR Imaging of Aleutian Volcanoes: Monitoring a Volcanic Arc from Space*, Springer; doi:10.1007/978-3-642-00348-6.

Lu, Z., D. Dzurisin, J. Biggs, C. Wicks, and S. McNutt (2010), Ground surface deformation patterns, magma supply, and magma storage at Okmok volcano, Alaska, from InSAR analysis: 1. Interruption deformation, 1997–2008, *J. Geophys. Res. Sol. Earth*, *115*(B5), B00B02; doi:10.1029/2009jb006969.

Lu, Z., D. Mann, J.,Freymueller, and D. Meyer (2000), Synthetic aperture radar interferometry of Okmok volcano, Alaska: Radar observations, *J. Geophys. Res.*, *105*, 10791–10806.

Lu, Z., H. S. Jung, L. Zhang, W. J. Lee, C. W. Lee, and D. Dzurisin (2013), Advances in mapping from aerospace imagery: Techniques and applications, in *DEM generation from satellite InSAR*, edited by X. Yang and J. Li, 119–144, CRC Press, New York.

Lu, Z., T. Masterlark, and D. Dzurisin (2005), Interferometric Synthetic Aperture Radar (InSAR) study of Okmok volcano, Alaska, 1992–2003: Magma supply dynamics and post-emplacement lava flow deformation, *J. Geophys. Res.*, *110*, B02403; doi:10.1029/2004JB003148.

Lu, Z., T. Masterlark, D. Dzurisin, R. Rykhus, and C. Wicks, Jr. (2003), Magma supply dynamics at Westdahl volcano, Alaska, modeled from satellite radar interferometry, *J. Geophys. Res.*, *108*(B7), 2354; doi:10.1029/2002jb002311.

Lyons, S., and D. Sandwell (2003), Fault creep along the southern San Andreas from interferometric synthetic aperture radar, permanent scatterers, and stacking, *J. Geophys. Res. Sol. Earth 108*(B1); doi: 10.1029/2002jb001831.

Mann, D., and J. Freymueller (2003), Volcanic and tectonic deformation on Unimak Island in the Aleutian Arc, Alaska, *J. Geophys. Res.*, *108*(B2), 2108; doi:10.1029/2002jb001925.

Marquardt, D. W. (1963), An algorithm for least-squares estimation of nonlinear parameters, *J. Soc. Ind. App. Math.*, *11*(2), 431–441; doi:10.2307/2098941.

Massonnet, D., and K. L. Feigl (1998), Radar interferometry and its application to changes in the Earth's surface, *Rev. Geophys.*, *36*(4), 441–500.

Masterlark, T. (2007), Magma intrusion and deformation predictions: Sensitivities to the Mogi assumptions, *J. Geophys. Res.Sol. Earth*, *112*(B6); doi: 10.1029/2006jb004860.

Mctigue, D. F. (1987), Elastic stress and deformation near a finite spherical magma body: resolution of the point-source paradox, *J. Geophys. Res. Sol.*, *92*(B12), 12931–12940.

Meyer, F., and J. Nicoll (2008), Mapping ionospheric TEC using Faraday rotation in full- polarimetric L-band SAR data, *Synthetic Aperture Radar (EUSAR), 2008 7th European Conference on*, 1–4.

Mogi, K. (1958), Relations between the eruptions of various volcanoes and the deformations of the ground surfaces around them, paper presented at Bulletin of the Earthquake Research Institute, Earthquake Research Institute, University of Tokyo.

Mosegaard, K., and A. Tarantola (1995), Monte-Carlo sampling of solutions to inverse problems, *J. Geophys. Res. Sol. Earth. 100*(B7), 12431–12447; doi: 10.1029/94jb03097.

Okada, Y. (1985), Surface deformation due to shear and tensile faults in a half-space, *Bull. Seism. Soc. Amer.*, *75*(4), 1135–1154.

Press, W. H., S. A. Teukolsky, W. T. Vetterling, and B. P. Flannery (2007), *Numerical Recipes in C : The Art of Scientific Computing*, 3rd ed., Cambridge University Press, Cambridge, New York.

Rosen, P. A., S. Hensley, H. A. Zebker, F. H. Webb, and E. J. Fielding (1996), Surface deformation and coherence measurements of Kilauea volcano, Hawaii, from SIR-C radar interferometry, *J. Geophys. Res. Planet*, *101*(E10), 23109–23125; doi: 10.1029/96je01459.

Rosen, P. A., S. Hensley, I. R. Joughin, F. K. Li, S. N. Madsen, E. Rodriguez, and R. M. Goldstein (2000), Synthetic aperture

radar interferometry: Invited paper, *P. IEEE*, *88*(3), 333–382; doi: 10.1109/5.838084.

Simons, M., and P. Rosen (2007), Interferometric Synthetic Aperture Radar Geodesy, in *Treatise on Geophysics*, edited by G. Schubert, 391–446, Elsevier Press, Amsterdam; Boston.

SRTM (2015), Enhanced Shuttle Land Elevation Data (http://www2.jpl.nasa.gov/srtm/).

Sudhaus, H., and S. Jonsson (2009), Improved source modelling through combined use of InSAR and GPS under consideration of correlated data errors: application to the June 2000 Kleifarvatn earthquake, Iceland, *Geophys. J. Int.*, *176*(2), 389–404; doi: 10.1111/j.1365-246X.2008.03989.x.

VHP (2015), USGS Volcano Hazards Program (http://volcanoes.usgs.gov/).

Williams, C. A., and G. Wadge (1998), The effects of topography on magma chamber deformation models: Application to Mt Etna and radar interferometry, *Geophys. Res. Lett.*, *25*(10), 1549–1552; doi: 10.1029/98gl01136.

Williams, C. A., and G. Wadge (2000), An accurate and efficient method for including the effects of topography in three-dimensional elastic models of ground deformation with applications to radar interferometry, *J. Geophys. Res. Sol. Earth*, *105*(B4), 8103–8120; doi: 10.1029/1999jb900307.

Wright, T. J., B. E. Parsons, J. A. Jackson, M. Haynes, E. J. Fielding, P. C. England, and P. J. Clarke (1999), Source parameters of the 1 October 1995 Dinar (Turkey) earthquake from SAR interferometry and seismic bodywave modelling, *Earth Planet. Sci. Lett.*, *172*(1–2), 23–37; doi: 10.1016/S0012-821x(99)00186-7.

Wright, T. J., Z. Lu, and C. Wicks (2003), Source model for the M w 6.7, 23 October 2002, Nenana Mountain earthquake (Alaska) from InSAR, *Geophys. Res. Lett.*, *30*(18), 1974; doi:10.1029/2003gl018014.

Wright, T. J., B. E. Parsons, and Z. Lu (2004), Toward mapping surface deformation in three dimensions using InSAR, *Geophys. Res. Lett.*, *31*(1); doi: 10.1029/2003gl018827.

Yang, X. M., P. M. Davis, and J. H. Dieterich (1988), Deformation from inflation of a dipping finite prolate spheroid in an elastic half-space as a model for volcanic stressing, *J. Geophys. Res. Sol.*, *93*(B5), 4249–4257; doi: 10.1029/Jb093ib05p04249.

Yun, S., P. Segall, and H. Zebker (2006), Constraints on magma chamber geometry at Sierra Negra Volcano, Galápagos Islands, based on InSAR observations, *J. Volcanol. Geotherm. Res.*, *150*(1–3), 232–243; doi:10.1016/j.jvolgeores.2005.07.009.

Zhang, L., X. Ding, Z. Lu, H.-S. Jung, J. Hu, and G. Feng (2014), A novel multitemporal InSAR model for joint estimation of deformation rates and orbital errors, *IEEE Trans. Geosci. Remote Sens.*, *52*(6), 3529–3540; doi:10.1109/tgrs.2013.2273374.